The Cryosphere

Vertical profile of the specific surface area and density of the snow at Dome C and on a transect to Dumont D'Urville, Antarctica – albedo calculations and comparison to remote sensing products

J.-C. Gallet, F. Domine, L. Arnaud, G. Picard, and J. Savarino

CNRS-INSU – Laboratoire de Glaciologie et Géophysique de l'Environnement, UMR5183,
54 rue Moliere, 38402 Saint-Martin d'Hères cedex, France

Université Joseph Fourier, Grenoble I, France

Abstract. The specific surface area (SSA) of snow determines in part the albedo of snow surfaces and the capacity of the snow to adsorb chemical species and catalyze reactions. Despite these crucial roles, almost no value of snow SSA are available for the largest permanent snow expanse on Earth, the Antarctic. We report the first extensive study of vertical profiles of snow SSA near Dome C (DC: 75°06′ S, 123°20′ E, 3233 m a.s.l.) on the Antarctic plateau, and at seven sites during the logistical traverse between Dome C and the French coastal base Dumont D'Urville (DDU: 66°40′ S, 140°01′ E) during the Austral summer 2008–2009. We used the DU-FISSS system, which measures the IR reflectance of snow at 1310 nm with an integrating sphere. At DC, the mean SSA of the snow in the top 1 cm is $38 \, \mathrm{m^2 \, kg^{-1}}$, decreasing monotonically to $14 \, \mathrm{m^2 \, kg^{-1}}$ at a depth of 50 cm. Along the traverse, the snow SSA profile is similar to that at DC in the first 600 km from DC. Closer to DDU, the SSA of the top 5 cm is $23 \, \mathrm{m^2 \, kg^{-1}}$, decreasing to $19 \, \mathrm{m^2 \, kg^{-1}}$ at 50 cm depth. This difference is attributed to wind, which causes a rapid decrease of surface snow SSA, but forms hard windpacks whose SSA decrease more slowly with time. Since light-absorbing impurities are not concentrated enough to affect albedo, the vertical profiles of SSA and density were used to calculate the spectral albedo of the snow for several realistic illumination conditions, using the DISORT radiative transfer model. A preliminary comparison with MODIS data is presented and our calculations and MODIS data show similar trends.

1 Introduction

High latitude regions play a crucial role in determining the climate of the Earth and its evolution (Goody, 1980; Warren, 1982; Hall, 2004; Lemke et al., 2007), because these regions are snow-covered most of the time and snow is the Earth's surface type with the highest albedo.

Discussions about snow albedo can be more detailed if one considers the spectral albedo, i.e. the fraction of solar light that is reflected as a function of wavelength. Figure 1 shows typical examples of snow spectral albedo, the examples chosen being those of pure recent snow, aged pure snow, and recent snow contaminated with absorbing impurities such as soot (also called black carbon).

Figure 1 illustrates that in the visible part of the solar spectrum, snow albedo is mostly determined by impurities (Warren and Wiscombe, 1980) while in the infra-red, grain size is the main factor affecting albedo (Wiscombe and Warren, 1980; Colbeck, 1982). Determining the spectral albedo of snow therefore requires the knowledge of snow grain size and impurity content.

Snow is a porous medium made of air and ice. Its physical properties evolve over time through processes grouped under the term "snow metamorphism" (Colbeck, 1982). Because ice has an elevated water vapor pressure (165 Pa at −15 °C and 610 Pa at 0 °C), and because the vertical temperature gradient almost always present in the snow generates sublimation-condensation cycles that modify the shapes and sizes of snow grains, the physical properties of snow change during metamorphism. These properties include density, thermal conductivity, permeability, but also albedo (Colbeck, 1982). Since snow grain size almost always increases during metamorphism (Cabanes et al., 2003; Legagneux et
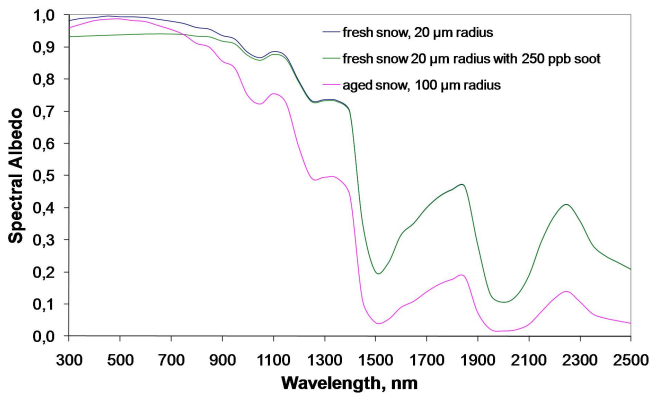
Fig. 1. Spectral albedo of fresh and aged pure snow and of fresh snow contaminated by soot. The plots were calculated using the DISORT radiative transfer code, which simulates snow grains as disconnected spheres of the radius indicated.

al., 2004; Flanner and Zender, 2006; Taillandier et al., 2007), snow albedo usually decreases during metamorphism. Understanding snow grain size and its variations is therefore crucial to predict snow albedo and to understand the energy balance of the Earth.

In many previous studies, snow grain size has been used as a key variable to describe interactions between snow and solar radiation (Warren, 1982; Alley, 1987; Grenfell et al., 1994). However, the notion of "snow grain size" is not very well defined, and varies from one study to another (Aoki et al., 2000). More recent studies have therefore used the surface/volume ratio of snow grains, i.e. the snow specific surface area (SSA), to calculate their optical properties. The SSA of snow is a measure of the area of the ice-air interface per unit mass (Legagneux et al., 2002).

$$\text{SSA} = \frac{S}{M} = \frac{S}{\rho_{ice} \cdot V} = \frac{3}{\rho_{ice} \cdot r_{eff}} \qquad (1)$$

with S the surface area of snow grains, M their mass, V their volume and ρ_{ice} the density of ice (917 kg m^{-3} at 0 °C). If snow crsytals are assumed to be spheres, then the above equation related the sphere radius r_{eff} to SSA. For non-spherical particles, Eq. (1) defines their effective (or optical) radius from their SSA. SSA is often expressed in units of m^2 kg^{-1} and measured values are in the range 2 m^2 kg^{-1} for melt-freeze crusts to 156 m^2 kg^{-1} for fresh dendritic snow (Domine et al., 2007b).

Theoretical studies have shown that for a given SSA, snow reflectance and albedo depend on crystal shape (Grenfell and Warren, 1999; Grenfell et al., 2005; Neshyba et al., 2003; Picard et al., 2009). However, for natural snow, comparisons between SSA measured by CH$_4$ adsorption and reflectance at 1310 nm found no effect of grain shape on reflectance, for a given SSA (Gallet et al., 2009). This is probably because snow grains are made up of a mixture of shapes, and the shape effects average out. Very recently, Ar-

naud et al. (2011) also used SSA values measured by CH$_4$ adsorption to model snow reflectance at 1310 nm, using the formalism of Kokhanovsky and Zege (2004), which uses a shape-dependent coefficient, b, to calculate reflectance for a given SSA. They found that the best fit was obtained for a b value of 4.56, very close to and within experimental error of the b value recommended for disconnected spheres ($b_{sphere} = 4.53$) by Kokhanovsky and Zege (2004). Based on both these studies we conclude that the reflectance of natural snow, which again is made up of a mixture of shapes, can adequately be modeled by approximating snow with disconnected spheres having the same SSA as the snow. Snow SSA therefore appears to be a convenient variable to study snow optical properties.

In early snow studies, there was no simple and reliable method to measure snow SSA, which is why "grain size" was used. Systematic measurements of snow SSA during field campaigns started when the methane (CH$_4$) adsorption technique was developed (Legagneux et al., 2002; Domine et al., 2007b). However, that method is time-consuming and requires liquid nitrogen, a problem in many field studies, so that its use remained confidential. Other methods such as stereology and X-Ray tomography, as reviewed in Domine et al. (2008), offer little advantage over CH$_4$ adsorption and present their own shortcomings. This probably explains why almost no data is available on the SSA of snow on polar ice caps. To help fill that data gap, optical methods to measure SSA have been recently developed (Gallet et al., 2009; Matzl and Schneebeli, 2006; Painter et al., 2007; Arnaud et al., 2011) to rapidly measure SSA in the field. These methods are based on the relationship between the IR reflectance of snow and its SSA (Domine et al., 2006). Here we will use the method of Gallet et al. (2009). It operates at 1310 nm, while the photographic method of Matzl and Schneebeli (2006) works around 900 nm, and the spectroscopic method of Painter et al. (2007) is around 1030 nm. At those shorter wavelengths, the reflectance dependence on SSA is not as strong as at 1310 nm, so that a better accuracy is expected at 1310 nm (Gallet et al., 2009). The availability of SSA data on large polar ice caps appears urgent because new remote sensing algorithms have been proposed to retrieve optical radius or SSA from Antarctica (Scambos et al., 2007; Jin et al., 2008) and Greenland (Kokhanovsky and Schreier, 2009; Lyapustin et al., 2009) and these methods need to be validated with field measurements. SSA measurements in Antarctica would be particularly useful because on the Antarctic plateau, absorbing impurities are negligible (Warren and Clarke, 1990), so that snow albedo can be calculated from SSA and density, if a planar snow surface is assumed.

Snow SSA is also an important variable to understand snowpack chemical composition and photochemistry and its impact on the composition of the polar boundary layer (Domine and Shepson, 2002; Grannas et al., 2007). Snow adsorbs many chemical species such as volatile and

semi-volatile compounds, and also species with a high dipole moment such as acidic gases that can establish hydrogen bonds with ice surfaces. Numerous authors have suggested that snow SSA largely determines the partitioning of many species between the snow and the boundary layer (Houdier et al., 2002; Herbert et al., 2006; Domine et al., 2007a; Burniston et al., 2007; Taillandier et al., 2006; Domine et al., 1995). The nitrate ion, possibly the main driver of snowpack photochemistry (Grannas et al., 2007), is thought to come to a large extent from the adsorption of atmospheric nitric acid (Domine and Thibert, 1996; Cox et al., 2005), and its concentration in snow would then be determined by snow SSA (Domine et al., 2008).

This work presents the first extensive measurements of the SSA of surface and near-surface snow on the Antarctic plateau near the Concordia station at Dome C (DC: 75°06′ S, 123°20′ E, 3233 m a.s.l.) and on the logistics traverse route between DC and the Dumont D'Urville base (DDU: 66°40′ S, 140°01′ E, 10 m a.s.l.) during the Austral summer campaign in 2008–2009. Near the DC base, measurements were performed in pits at least 70 cm deep where SSA, density and the thickness of snow layers were measured in detail. During the traverse, the main objective was of logistical nature. Scientific objectives were not initially planned and were added at the last minute. Measurements are therefore fewer and limited to a depth of 50 cm. They are nevertheless presented because of their uniqueness.

The data presented here show the vertical profiles of SSA and allow applications to radiative transfer and atmospheric chemistry. We chose here to limit our discussion to radiative transfer and use the DISORT model (Stamnes et al., 1988) to calculate snow spectral albedo representative of the Antarctic plateau, in order to provide data that can in future be compared to satellite retrievals and used to test SSA or optical radius retrieval algorithms.

2 Methods and study site

For clarity, measurements at DC and during the traverse will be presented separately. Pits done at DC are named C1 to C13 and pits done during the traverse are named T1 to T8. For each pit, a flat area was chosen and a clean face was obtained with a saw and a brush to minimize disturbance to the stratigraphy and to remove loose particles. The stratigraphy was carefully observed and the SSA, density and thickness of all layers was measured.

Density was measured by weighing a snow core of known volume. For thick layers of low to moderate hardness, a 500 cm^3 plexiglas coring tube was used. For thin or hard layers, a 100 cm^3 stainless steel coring tube was used. Density was measured for each layer, with a vertical resolution of 10 cm or better, depending on the number of layers. The error on density measured with a coring tube is about 5 % (Conger and McClung, 2009).

The thickness of layers was measured with a ruler. The accuracy of a reading is 2 mm and is slightly observer-dependent because the boundaries between layers were usually not sharp. Furthermore, the thickness of layers was horizontally variable, so that on average the thickness of a layer varied by 10 % over a width of 1 m.

SSA was measured using the DUFISSS (DUal Frequency Integrating Sphere for Snow SSA measurements) instrument described in Gallet et al. (2009). Two aspects need to be briefly reminded here: the sampling protocol and the SSA measurement method. For sampling, a special coring tool was used to sample a cylindrical snow core 63 mm in diameter and 30 mm in height. The snow core was pushed gently with a piston into the cylindrical sample holder 63 mm in diameter and 25 mm deep, so that 5 mm of snow stick out of the sample holder. This extra snow is shaved off with a sharp spatula just before the measurement. This sampling procedure was designed to minimize the perturbation to the snow. For soft surface layers, the objective was whenever possible to measure SSA with a 1 cm resolution. In that case, the top 1 cm was sampled with a spatula and placed in the sample holder. Additional surface snow was placed in the sample holder until it was full. The soft snow was gently compacted to fill any voids and, if required, the surface was shaved clean as previously mentioned. Tests revealed that for soft snow such handling did not affect the IR reflectance. For hard windpacks, the small particles generated by shaving were gently brushed off. Of course, at Dome C and during the traverse, temperatures were such that no liquid water was ever present.

The sample was then illuminated with a 1310 nm laser diode and the reflected light was collected with an integrating sphere 15 cm in diameter. The signal was measured with an InGaAs photodiode. The signal was converted to reflectance using a set of six standards of reflectances between 4 and 99 %. The reflectance was converted to SSA using a calibration curve obtained with snow samples whose SSA was measured using CH_4 adsorption and reflectance measured with DUFISSS (Gallet et al., 2009). The accuracy of these measurements is 10 %. The e-folding depth (hereafter penetration depth, PD) of the 1310 nm radiation in typical Antarctic snow is of the order of 1 cm. For example radiative transfer calculations using methods described in Sect. 4 show that for recent snow (density = 120 kg m^{-3}, SSA = 40 m^2 kg^{-1}), PD = 8 mm, and for Antarctic depth hoar (density = 230 kg m^{-3}, SSA = 12 m^2 kg^{-1}), PD = 9 mm. Our method therefore gives a weighted average of SSA over about a 1 cm depth. The accuracy of SSA measurements with DUFISSS is 10 %.

At Dome C, snow layers remain a long time near the surface after precipitation because of the very low accumulation rate: 26 mm water equivalent (Frezzotti et al., 2005). Snow layers are frequently remobilized by wind, whose mean speed is 6 m s^{-1}, with maximum values of the order of 15 m s^{-1} (Frezzotti et al., 2005).
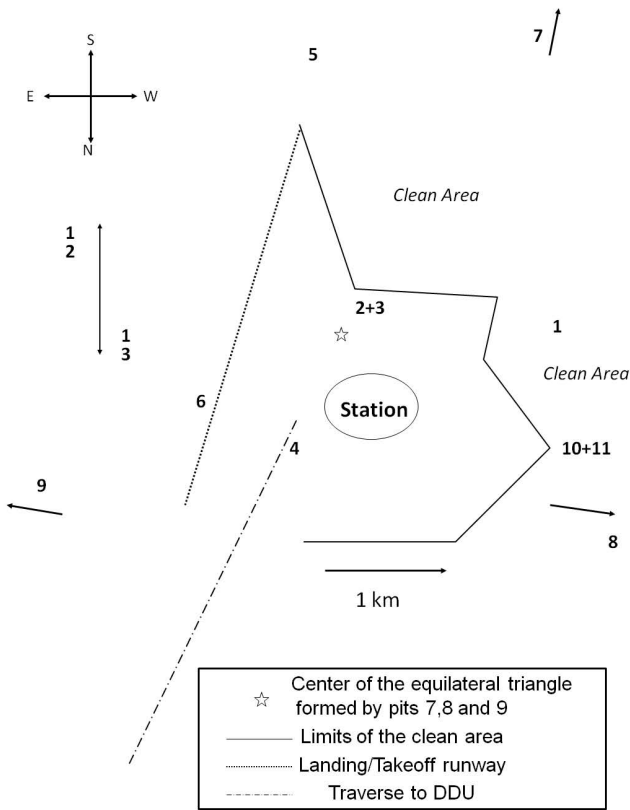
Fig. 2. Location of group C pits around Concordia station at Dome C, 75°06′00.2 S, 123°19′58.8 E.

Measurements at DC focused on surface snow layers, because their effect on albedo is greatest. SSA measurements were performed at depths of 1, 2, 5, 10 and 15 cm. Further down, each observed layer was measured once with a minimal resolution of 10 cm. During the traverse, less time was available for the measurements and only one measurement was performed in the top 5 cm.

3 Results

3.1 Dome C

At DC, thirteen pits C1 to C13, with depths between 70 and 100 cm, were studied. Figure 2 and Table 1 show the location and coordinates of these pits.

To facilitate the comparison between the pits, we present here the data on the top 70 cm of each pit. SSA, density and depth of each layer are detailed in Appendix Table A1. The variability of the stratigraphy is adequately represented by the three stratigraphic profiles of pits C2, C3 and C7, shown in Fig. 3.

The stratigraphy of pit C2 is as follows: the surface layer is comprised of small rounded grains recently deposited by the wind, overlying a 3 cm-thick hard windpack. Below that, we

observed a layer of faceted crystals, and then a thick layer of depth hoar, briefly interrupted by a 3 cm-thick layer of mixed-form crystals between 34 and 37 cm below the surface. In pit C3, the surface layer is 2 cm thick and comprised of a mixtures of small rounded grains transported by the wind and surface hoar crystals. Below, windpacks and faceted crystals or mixed-form crystals alternate. Finally, the top 1-cm thick surface layer in pit C7 is a mixture of surface hoar, faceted crystals and small rounded grains. The rest of the pit is mostly comprised of mixed-form crystals, interrupted by a windpack between 25 and 46 cm. For all pits except C1 and C2, the SSA was measured for the top 1 cm, the second cm, then at 5, 10, 15 and 20 cm, and subsequently every 10 cm. For C1 and C2, the top 5 cm appeared homogeneous and only one measurement was performed on this top layer. For consistency, the SSA determined is attributed to the depths of 1, 2 and 5 cm. Figure 4 shows that in the top 15 cm of the snow, SSA values span a fairly wide range depending on the snow pit: 13 to 56 m^2 kg^{-1}. Below that, the range of SSA values narrows down, except for pits C12, C3 et C7 where values at 20 cm are respectively 24, 28 and 39 m^2 kg^{-1} while for the other ten pits the range is 13 to 21 m^2 kg^{-1}. For the three outlying pits, the layer at 20 cm is either a windpack or faceted crystals, but in all cases is very hard.

Figure 4 also illustrates the mean SSA profile, showing that SSA values decrease monotonically in the first 70 cm. Because of the three outlying pits, the mean values between 15 and 40 cm are higher than the SSA of most pits.

Figure 5 shows the density values for all C pits. There is a significant scatter, but the average profile shows a monotonic increase from the surface to 15 cm, followed by an essentially constant density near 350 $kg\,m^{-3}$. A thick very hard windpack explains the densities greater than 500 $kg\,m^{-3}$ in pit C10.

In summary, in group C pits, density and SSA are highly variable in the top 15 cm. Below that, most values fall within a fairly narrow range, except when windpacks or other hard layers are present where higher densities and SSA values are observed.

3.2 Logistics traverse between Dome C and Dumont D'Urville

Group T pits were studied during the 8-day traverse (2 to 10 February 2009) and are named T1 to T8. Because of bad weather there is no pit T6. Figure 6 shows the traverse between DC and DDU and the location of the pits, as well as the automatic weather stations (AWS) D85, D47 and D10 used to interpret pit observations.

T group pits are shallow (50 cm) because little time was available each evening for work. Moreover, the frequent strong winds had often produced very hard windpacks that slowed down the work and only one pit could be done each evening. Given the spatial variability of the snow observed at DC, the number of pits is insufficient for a good

Table 1. Coordinates of group C and T pits.

Pit Number	Date of measurement	South Coordinate	East Coordinate	Observations	Comments
C1	24 November 2008	75°06′14.4″	123°17′50.5″	Clear sky	
C2	2 December 2008	75°06′16.4″	123°20′10.8″	Clear sky	2 and 3 are within 20 m from each other
C3	4 December 2008	75°06′16.4″	123°20′10.8″	Cloudy	
C4	15 December 2008	75°05′51.6″	123°21′32.1″	Clear sky	
C5	17 December 2008	75°07′03.4″	123°20′26.7″	Clear sky	
C6	23 December 2008	75°06′13.8″	123°21′54.0″	Clear sky	
C7	26 December 2008	75°08′01.0″	123°16′08.0″	Clear sky	*
C8	9 January 2009	75°03′51.0″	123°14′48.1″	Clear sky at 09:00 UTC	*
C9	13 January 2009	75°06′49.8″	123°28′30.1″	Clear sky	*
C10	24 December 2008	75°05′56.3″	123°18′00.0″	Few Cirrus	American tower
C11	4 December 2008	75°05′56.3″	123°18′00.0″	Cirrus	American tower
C12	3 January 2009	75°19′16.0″	123°24′01.1″	Overcast	25 km South
C13	4 January 2009	74°32′41.0″	123°23′43.0″	Overcast	25 km North
T1	2 February 2009	74°10′20.5″	126°03′10.4″	Overcast	Altitude 3216 m
T2	3 February 2009	73°08′29″	128°35′55″	Overcast	Altitude 3169 m
T3	4 February 2009	72°01′58″	131°05′26″	Cirrus	Altitude 3049 m
T4	5 February 2009	70°53′16″	133°17′07″	Clear sky, Drift	Altitude 2798 m
T5	6 February 2009	69°49′36″	134°12′07″	Clear sky	Altitude 2600 m
T6	7 February 2009	68°44′49″	134°54′21″	No pit (windy)	Altitude 2430 m
T7	8 February 2009	68°00′53″	136°27′52″	Overcast	Altitude 2060 m
T8	9 February 2009	67°24′53″	138°36′06″	Clear sky	Altitude 1585 m

* C7, C8 and C9 are approximately at 5 km from the base. An equilateral triangle is formed by those three pits, the center is the star on Fig. 2.

representativity. However, they are the only SSA data available for this region. The exact pit site was chosen somewhat arbitrarily. Basic safety considerations imposed that the pit be within 500 m of the convoy. Within this range, a planar and homogeneous area of at least $10\,m^2$ was chosen. As for the Dome C pits, we first present the stratigraphy of selected pits (Fig. 7), before presenting SSA and density data. Detailed data are reported in Appendix Table A2.

At the top of pit T2, a 10 cm-thick windpack was observed. Below that was a 3 cm layer of mixed-form crystals, then a 1 cm windpack, and finally distinct layers of faceted crystals extending down to 70 cm. Pit T5 was comprised of windpacks, except between 7 and 11 cm, where a softer layer of small rounded grains was observed, and between 14 and 34 cm where a layer of mixed-form crystals was found. Overall, the snow stratigraphy along the traverse showed little variability and only five crystal types were observed.

SSA values are shown in Fig. 8, as well as the average of the T pits. In all pits except T1 the top layer was hard and appeared homogeneous over at least the top 5 cm. It was not possible to sample separately the top 1st and 2nd cm and only one SSA measurement was made in the top 5 cm. However, for comparison with C pits, this one value is attributed to depths of 1, 2, and 5 cm in Fig. 8. SSA values in the top 5 cm range from $20\,m^2\,kg^{-1}$ to $38\,m^2\,kg^{-1}$. Below, in general the SSA is less homogeneous than at DC. Noteworthy observations include: (a) in pit T2, SSA varies by a factor of 1.8 between 40 and 50 cm even though a single layer was observed; (b) pits T4 and T5 show fairly constant SSA values around $23\,m^2\,kg^{-1}$ below 15 cm; (c) pits T1 to T4, closer to DC, have SSA values in the top 15 cm that are above the group average, while in pits T5 to T8, which are closer to DDU, top values are all below average, (d) the general trend is that SSA decreases with depth, especially in the top 20 cm.

Density values, reported in Fig. 9, show a very high inter-pit variability. Near the surface, values range between $162\,kg\,m^{-3}$ (T1) and $446\,kg\,m^{-3}$ (T8), and the range is even larger at 10 cm (150 to $515\,kg\,m^{-3}$) and remains high at 50 cm (272 to $478\,kg\,m^{-3}$). The general trend is that density increases from DC to DDU. However, for a given pit, there is little density increase with depth, as further illustrated by the average trend also reported in Fig. 9.

3.3 SSA and density profiles representative of Antarctic plateau snow

Figures 8 and 9 indicate that pits T1 to T4, closer to DC, show high SSAs and low densities near the surface, while pits T5 to T8 have low SSAs and high densities. At depths around 40 cm, higher SSAs and densities are observed in pits T5–T8. It therefore appears sensible to separate the traverse data into two classes: T1–T4 and T5–T8. Rather than consider mean values for the whole traverse, it makes more sense to look at averages for both these classes, as done in Figs. 10 and 11.
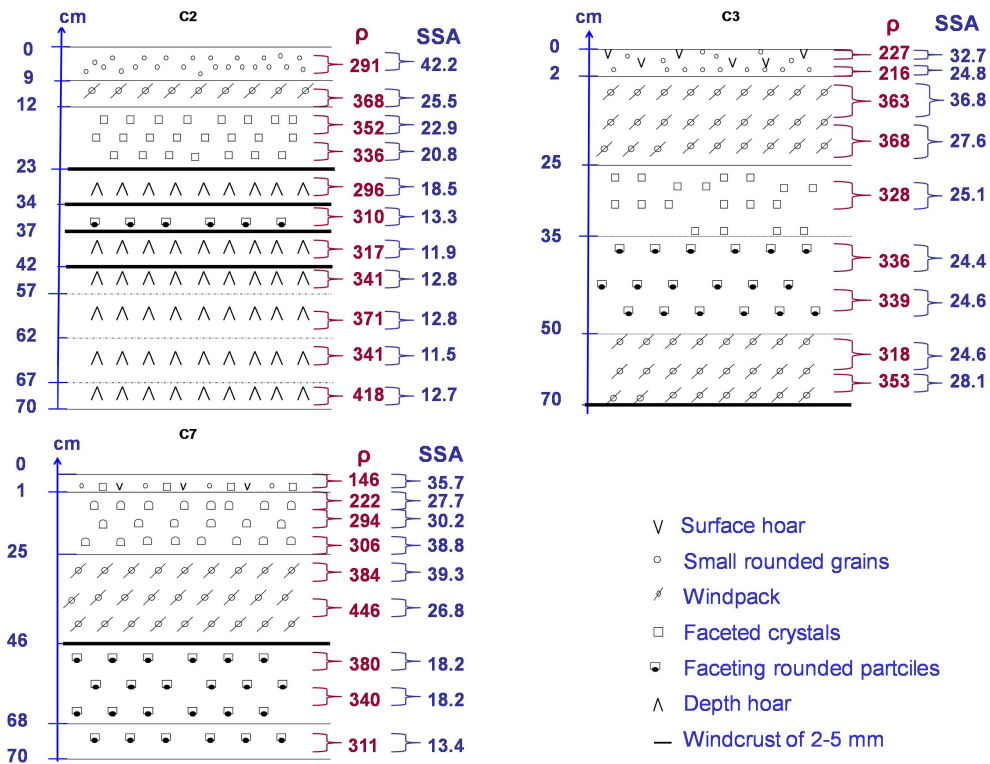
Fig. 3. Stratigraphy, density (ρ) in kg m^{-3} and SSA in m^2 kg^{-1} of pits C2, C3 and C7.
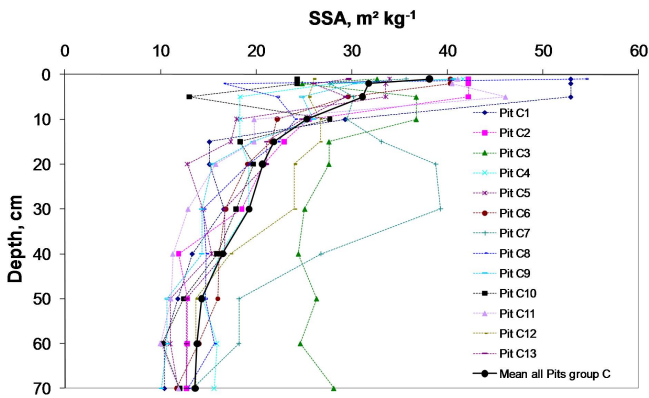

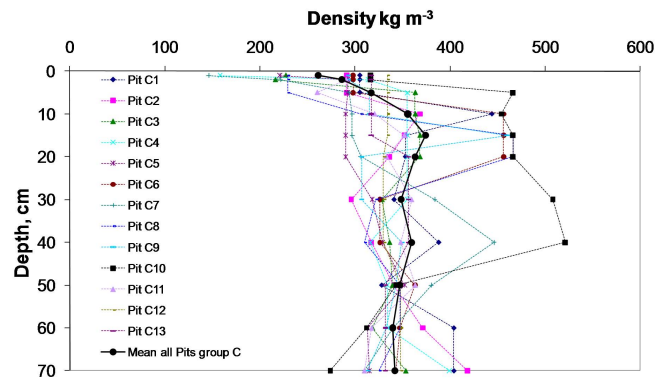**Fig. 4.** SSA profiles of group C pits at Dome C.

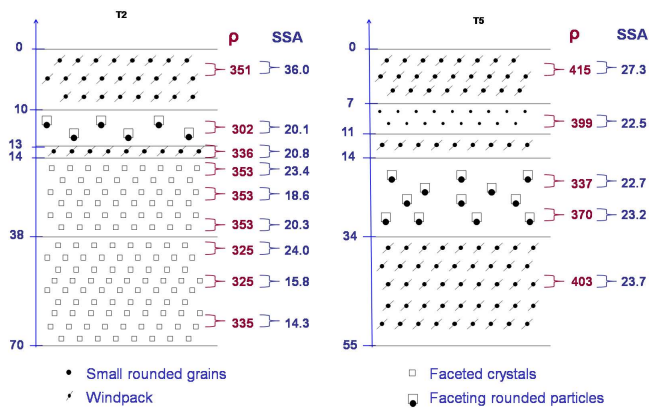**Fig. 5.** Density profiles of group C pits at Dome C.

Figure 10 shows that SSA profiles of DC and T1–T4 are fairly similar. On the other hand, Fig. 11 shows that DC densities are greater than for T1–T4. The greater values of T1–T4 in the first 2 cm may simply be because for T pits, only one value was measured in the top 5 cm, and assigned to the three depths 1, 2 and 5 cm. Regarding the T5–T8 pits, Figs. 10 and 11 show that they have the highest densities at all depths, and that their SSAs are lower than elsewhere in the top 30 cm, and higher below that depth.

This brief description indicates that the mean snow physical properties investigated here show little variation around

DC, up to a distance of about 600 km towards DDU (T1–T4). Beyond that (T5–T8), SSAs are lower near the surface, while densities are higher. This conclusion is somewhat weakened by the small number of T pits, but the difference between both T sub-groups appears significantly greater than the intra-group variability, so we believe that the difference between both sub-groups is real. We suspect this is caused by different meteorological conditions, which influence snow metamorphism and the type of snow crystals formed. AWS temperature and wind speed data with 10 min resolution (available at ftp://amrc.ssec.wisc.edu/pub/aws/) are shown in
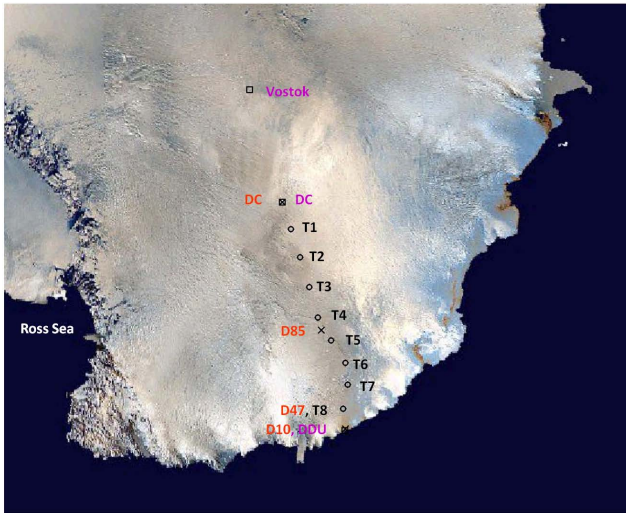
Fig. 6. Map of the logistical traverse between Dome C (DC) and Dumont D'Urville (DDU). The locations of all group T pits (circles) and automatic weather stations D85, D47 and D10 (X) are shown.

Fig. 7. Stratigraphy, density (ρ) in $\mathrm{kg\,m^{-3}}$ and SSA in $\mathrm{m^2\,kg^{-1}}$ of pits T2 and T5.
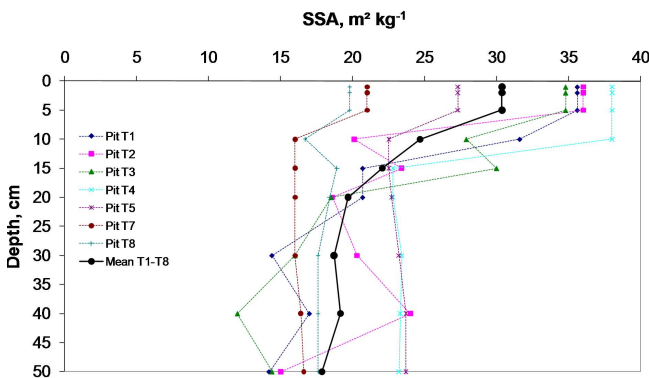
Fig. 8. SSA profiles of group T pits along the logistical traverse. There is no T6 pit because of bad weather that day.
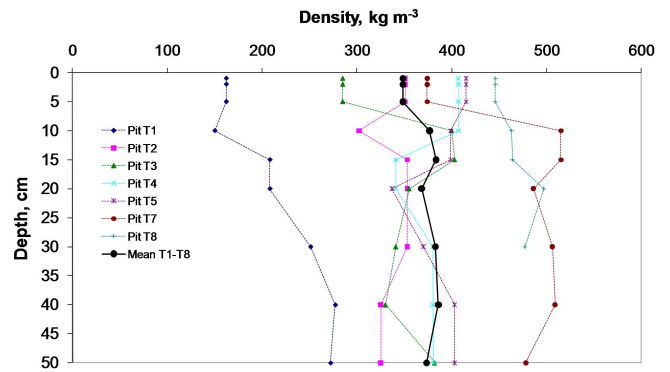
Fig. 9. Density profiles of group T pits along the logistical traverse.
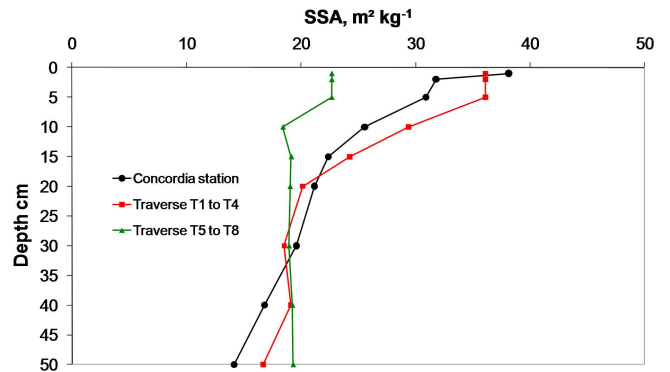
Fig. 10. Mean SSA profiles at DC and along the traverse.
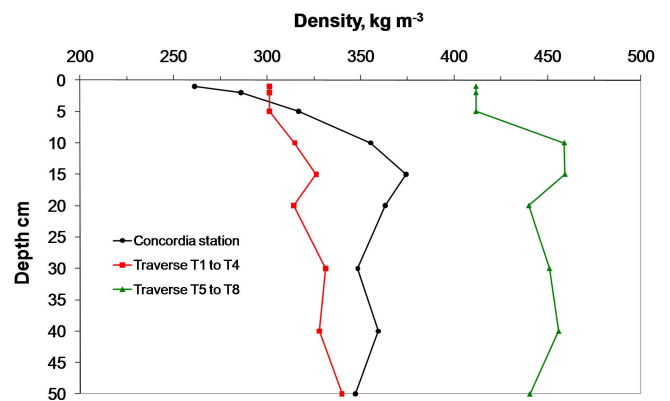
Fig. 11. Mean density profiles at DC and along the traverse.

Figs. 12 and 13 and confirm this suggestion. Temperature rises by 20 to 35 °C between DC and AWS D10, located a few km from the coast. Wind speed also increases, and in particular the intensity of extreme events that favor the formation of hard windpacks increases considerably. During the period considered, the highest wind speed at DC was 14 m s^{-1}, while it reached 28 m s^{-1} at D47. It may even have reached higher values at D10, but February data are missing.
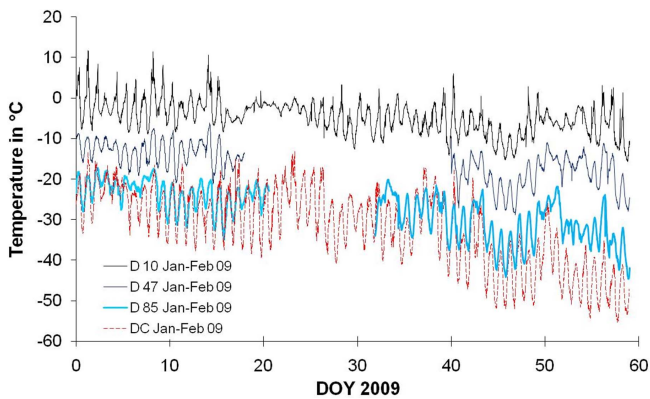
Fig. 12. Time series of temperature along the traverse in January and February 2009. DOY = Day Of Year. Data from AWSs.
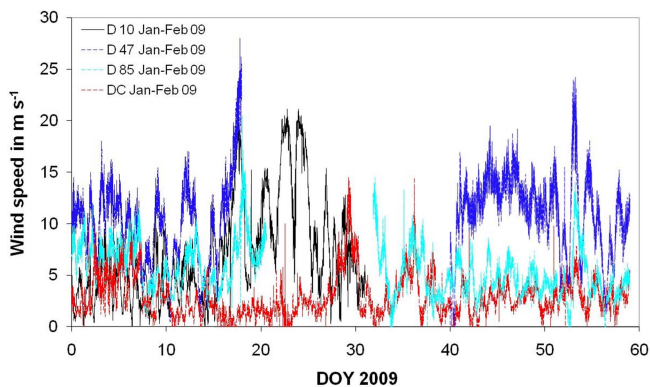
Fig. 13. Time series of wind speed along the traverse in January and February 2009. DOY = Day Of Year. Data from AWSs.

Do current data available on the rate of SSA decrease allow the understanding of the different behaviours shown in Figure 10? In general, snow SSA has been observed to decrease with time (Cabanes et al., 2003; Legagneux et al., 2004; Taillandier et al., 2007) although a few instances where SSA increases have been reported, and wind was often a factor in these increases (Domine et al., 2009). Models (Legagneux and Domine, 2005; Flanner and Zender, 2006) also predict that SSA should decrease with time. Temperature, temperature gradient, the SSA value and density are the main factors that are currently thought to affect the rate of SSA decrease. SSA decreases faster at higher temperatures and under higher temperature gradients. The experimental work of Taillandier et al. (2007) indicates that there is a temperature gradient threshold around $15\,\mathrm{K\,m}^{-1}$ separating two regimes for the rate of SSA decrease, the rate of decrease being significantly higher at higher gradients. The rate of decrease is also faster for higher SSAs. The impact of density is not clear and no experimental work is available on its effect. The model of Legagneux and Domine (2005) indicates that under isothermal conditions, higher densities accelerate SSA decrease be-

cause sinks and sources of water vapor are nearer. On the other hand, the model of Flanner and Zender (2006), which includes the effect of the temperature gradient, concludes that increasing density retards SSA decay, because water vapor migration in a more tortuous network is hindered. In any case, none of those studies treat many processes to which the snow was subjected to. These include the effects of wind and wind transport on SSA, and also the effect of diurnally alternating temperature gradients (Pinzer and Schneebeli, 2009). On the Antarctic plateau, the accumulation rate is so low that a given snow layer is exposed to wind action and alternating temperature gradients for a long time before it is finally sheltered from those effects. Fresh snow with high SSA can have its SSA drop dramatically faster because of wind (Cabanes et al., 2002). On the contrary, the remobilization of aged snow by wind can increase its SSA (Domine et al., 2009). The effect of alternating temperature gradients on the rate of SSA change has been little documented. Besides unexpected grain shapes (Pinzer and Schneebeli, 2009), this could lead to sublimation of snow grains and to condensation of atmospheric water vapor onto them, with effects on SSA that are difficult to predict. Today there is therefore insufficient data to understand the effect of many processes prevalent in Antarctica on snow SSA. Furthermore, no experiments have been performed at the low temperatures of the Antarctic plateau, and where the empirical equations of Taillandier et al. (2007) may not apply.

It therefore appears difficult to reach a satisfactory explanation for the SSA trends observed in Fig. 10. We must limit our conclusion to the following. Closer to the coast (T5 to T8), where winds are stronger, windpacks of high density form preferentially. These have a density around $430\,\mathrm{kg\,m}^{-3}$. Using the density-SSA correlation of Domine et al. (2007b) for tundra windpacks, the snowpack type studied by Domine et al. (2007b) closest to that observed here, predicts a SSA around $20\,\mathrm{m}^2\,\mathrm{kg}^{-1}$, as observed. Closer to DC (C group and T1 to T4 pits) there is a predominance of rounded grains near the surface, and the average density is about $280\,\mathrm{kg\,m}^{-3}$. The correspondence to tundra snow, again probably the snow type studied closest to that observed (Domine et al., 2007b), predicts a SSA of $28\,\mathrm{m}^2\,\mathrm{kg}^{-1}$, lower than the surface values found here, in the range 30 to $38\,\mathrm{m}^2\,\mathrm{kg}^{-1}$. We therefore conclude that in this type of snow, wind, although moderate, tends to increase snow SSA, presumably through transport, fragmentation and sublimation of grains, as described by Domine et al. (2009). We note furthermore that layers of faceted crystals observed here were significantly harder than found in seasonal snowpacks, so that processes involved in their formation and evolution may be different. More work on the effects of wind and low temperatures on SSA is required before we can understand the evolution of the SSA of the Antarctic surface snows studied here.

3.4 Antarctic snowpack spectral albedo modeling with DISORT

The SSA and density data obtained here can be used to calculate the optical properties of Antarctic snow. Since snow on the Antarctic plateau is almost free of light-absorbing impurities (Grenfell et al., 1994; Warren et al., 2006), its albedo over the solar spectrum is determined by its SSA and its density. Surface roughness can also have an important effect, but this manifests itself mostly in the calculation of directional reflectance (Leroux and Fily, 1998; Warren et al., 1998; Mondet and Fily, 1999) and much less in albedo calculations (Warren et al., 1998). Intuitively, this can be understood by considering a fictitious rough surface that would be totally reflective, under directional illumination. When looking at reflection in the forward direction, shading due to surface roughness will decrease the directional reflectance. On the contrary, if the albedo is considered, then all the photons will be reflected, regardless of surface structure, and the albedo will be unity, whatever the surface roughness. Of course snow is not fully reflective, so snow albedo is affected by surface roughness. However, at present, we are generally not capable of quantifying this effect, so that for example elaborate algorithms that retrieve grain size from satellite data simply neglect surface roughness (Fily et al., 1997; Kokhanovsky and Schreier, 2009). Here, we also neglect it. On the Antarctic plateau, this is probably a valid approximation, as sastrugi (i.e. snow dunes caused by wind, mostly through erosion processes) are small, at the most 10 cm. On the traverse, as we neared the coast, their height increased and often reached 30 cm, sometimes more, so that their possible effect must be kept in mind when interpreting model results.

Here, we present calculations of the directional hemispherical reflectance of the snow studied (according to the definition of Schaepman-Strub et al., 2006), and bi-hemispherical reflectance, referred to hereinafter as albedo for simplicity, with several incident radiations. One of the possible uses of these calculated albedos is the comparison to remote sensing data, in order to test inversion algorithms. We first detail how the DISORT code was used in our calculations.

3.5 The DISORT code

DISORT (Stamnes et al., 1988) treats snow as disconnected spheres and can model the reflectance of a succession of plane parallel snow layers under direct or diffuse illumination. Scattering and absorption efficiencies Q_{abs} and Q_{scatt} are calculated by the routine Mie0 (Wiscombe, 1980). The extinction efficiency $Q_{ext} = Q_{abs} + Q_{scatt}$ is thus obtained and allows the calculation, for each snow layer, of the dimensionless variable called the optical depth τ (Wiscombe and Warren, 1980):

$$\tau^i = \frac{3 Q_{ext}^i \rho_{snow}^i h^i}{4 a^i \rho_{ice}} \tag{2}$$

where a^i is the radius of the (spherical) snow particles of the ith snow layer, ρ_{snow}^i and h^i are the density and thickness of the i-th snow layer, and ρ_{ice} is the density of ice, $917\,\mathrm{kg\,m^{-3}}$ at $0\,^\circ$C. Given that for spherical particles we have $SSA^i = 3/(\rho_{ice} a^i)$, we obtain:

$$\tau^i = \frac{1}{4} Q_{ext}^i \cdot \rho_{snow}^i \cdot SSA^i \cdot h^i \tag{3}$$

A medium is considered optically semi-infinite when increasing its geometrical thickness modifies its albedo by less that 1 % (Wiscombe and Warren, 1980). From the optical depth τ, the single scattering albedo ω and the phase function $P(\Omega 1\ \Omega 2)$, DISORT calculates the albedo of the medium considered. Variations of these three variables depend only on wavelength and on grain size, i.e. SSA. Therefore, the evolution of the spectral albedo of semi-infinite snow formed of plane-parallel layers under given illumination conditions only depends on the SSA, density and thickness of each snow layer.

Zhou et al. (2003) showed that calculations of albedo better reproduce field observations if a multilayer snowpack, with layers having different SSAs and densities, is used. In a similar approach, we here use our observed vertical variations of SSA and density to calculate using DISORT the albedo of snow on the Antarctic plateau. We use the top 70 cm for snow at Dome C and the top 50 cm for snow of the traverse. With these depths and given Antarctic solar zenith angles, snow is mostly semi-infinite, but to minimize any error due to insufficient depth, we add to these snow stratigraphies a 2-m thick snow layer having the properties of the last layer measured.

3.6 DISORT configuration

In Antarctica, besides snow SSA and density, the factors that influence albedo are the type of illumination (direct or diffuse), the solar zenith angle (SZA), cloud cover, and surface roughness. As mentioned above, a general theoretical framework to quantify the effect of surface roughness on albedo does not exist, so we neglect it here. Justifications to neglect it include (1) we are dealing with albedo, so that the effects of surface roughness are considerably attenuated (Warren et al., 1998); (2) near Dome C, surface structure were only a few cm high; (3) most of our calculations use diffuse illumination, so that surface structures produce no shading.

Clouds enhance the diffuse fraction of radiation and absorb the IR fraction of the solar spectrum, leading to an increase in broad-band albedo because snow is less reflective in the IR (Fig. 1). Here, we do not investigate the effect of clouds on the spectral distribution of the incident radiation. We model the spectral albedo under direct illumination, clear sky conditions and totally overcast conditions. Clear sky conditions are represented by a direct incident radiation to which the diffuse component caused by Rayleigh scattering in the atmosphere has been added. Overcast conditions

Table 2. Name and type of incident light sources used in the DISORT calculations.

Source name	% Direct incident flux	% Diffuse incident flux	Solar zenith angle θ_i, degrees
DIR60	100	0	60
DIR70	100	0	70
DIFF	0	100, on all spectrum, Cloudy conditions	–
CS60	(100-diffuse)	Wavelength dependant, Eq. (4), Clear sky conditions	60
CS70	(100-diffuse)	Wavelength dependant, Eq. (4), Clear sky conditions	70

are represented by completely diffuse incident radiation over the whole solar spectrum.

Both the SZA (θ) and the type of illumination considerably affect snow albedo. The higher θ, the higher the albedo because snow is strongly forward scattering. Therefore, an incoming photon at high SZA penetrates less deeply in the snow and has a higher probability of exiting the snow (Warren, 1982). The albedo under diffuse illumination is approximately the same as that under direct illumination with $\theta = 50°$ for a semi-infinite medium composed by a single layer (Warren, 1982). Since at DC, the SZA is at least 52°, the albedo under direct illumination is always greater than that under diffuse illumination. Under clear sky conditions, there is always some diffuse light caused by atmospheric scattering. Grenfell et al. (1994) propose empirical relationships to determine the ratio of diffuse over total radiation (D/T) as a function of wavelength for Vostok and South Pole stations with clear sky. The relationships for both sites are different mainly because of their different altitudes. Taking into account the elevation of DC, which is intermediate between those of South Pole and Vostok, we estimate that at DC we have:

$$\frac{D}{T} = R_{\text{diffuse}} = 0.0249 \cdot \lambda^{-3.3} \tag{4}$$

where λ is the wavelength in µm. More rigorously, D/T also depends on SZA, but we neglect this effect here, since we subsequently limit our calculations to the cases when SZAs are 60 and 70°. Below, we calculate albedos for five illumination conditions, i.e. light sources: direct with 60 and 70° SZAs (light sources DIR60 and DIR70), diffuse (light source DIFF), and clear sky conditions with SZA of 60 and 70° (light sources CS60 and CS70), following Eq. (4). The characteristics of the five light sources are summed in Table 2. Subsequently, some of those calculations can be used for comparisons with satellite data. Since the latter data are obtained at a specific viewing angle, the comparison is not always simple, but correction factors between conical and
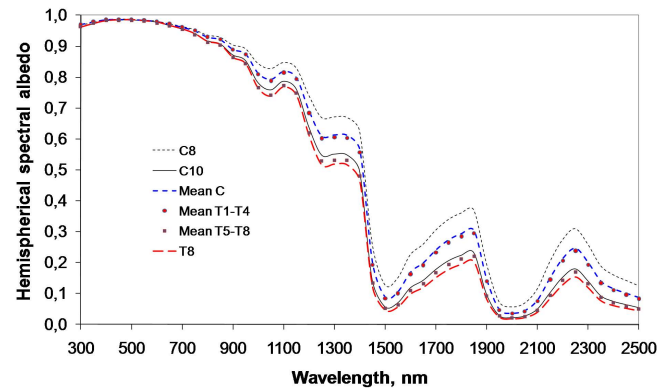
Fig. 14. Hemispherical spectral albedos calculated for selected snow pits of the C and T groups, using the DIR70diff source. Mean values for the three pit groups are also shown.

hemispherical reflectances have been proposed (Stroeve and Nolin, 2002; Kokhanovsky and Zege, 2004).

3.7 DISORT modeling at DC and along the logistical traverse

Figure 14 shows the range of calculated albedos for the C and T pits, illuminated with the CS70 source (see Table 2), as well as their averages. As expected (Warren, 1982), the albedo is high in the visible (>0.95) and shows little variations between different pits. Significant variations are observed in the IR, where, at a given wavelength, the albedo increases with the SSA of surface layers (Wiscombe and Warren, 1980).

The pit with the highest IR albedo is C8 because its surface layer has the highest SSA, fresh snow of $54.5 \, \text{m}^2 \, \text{kg}^{-1}$. Similar considerations explain why C10 has the lowest albedo: it has the lowest SSA in the top 10 cm. The mean value of C pits was obtained by performing calculations for a snow-pit with the average SSA and density at each depth. The
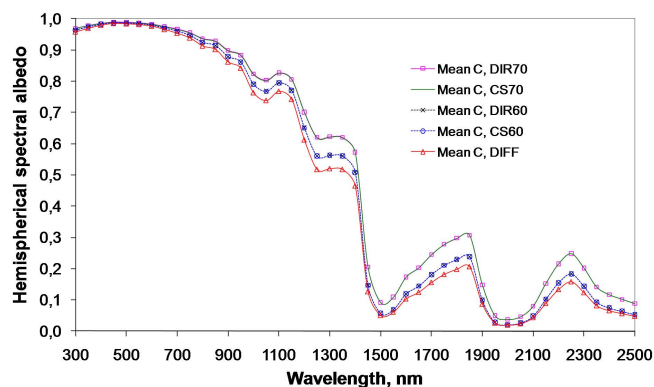
Fig. 15. Hemispherical spectral albedo of the mean group C snow pit, calculated with all light sources of Table 2.

variability, expressed as the difference between the mean and the extremes, is $\pm 1\%$ in the visible and reaches $\pm 40\%$ in the IR.

T1 to T4 pits (not shown in Fig. 14, for clarity) had similar albedos, calculated using the CS70 light source. This is because the SSAs of their surface layers fall in a narrow range, 34.8 to 38 $m^2\,kg^{-1}$. The albedo of the mean T1–T4 pit is very close to that of the mean C pit. T5 to T8 pits have lower albedos than the other T pits, because of the lower SSA of their surface layer. This is evidenced by the albedo of the average T5–T8 pit, which has the lowest average albedo. The T8 pit has the lowest albedo, because it has the lowest surface SSA, and it is also shown in Fig. 14.

Figure 14 shows that in the visible, the albedos of all pits are similar, because we neglected the effect of absorbing impurities. At 450 nm, the highest albedo is 0.989 and the lowest is 0.985, an undetectable difference. In the IR, relative differences between the albedos of pit C8 and pit T8 are 30% at 1250 nm and 218% at 1650 nm, which should be easily detectable.

Lighting conditions also affect significantly the albedo. Figure 15 illustrates the albedo of the mean C pit for the 5 illumination sources of Table 2. Figure 15 shows that the DIR60 and the CS60 light sources give essentially the same albedos. The same can be said of the DIR70 and CS70 sources.

3.8 Representative spectral albedo of the Antarctic plateau

The physical properties of the snow around Dome C show significant variations from pit to pit. However, we believe that the thirteen pits studied here within 25 km of the DC base capture the natural variability of the snow and that the spatially-averaged albedo of the snow is well represented by that of the mean C snow pit. Indeed, we were careful to study spots that featured the various snow types present near the surface: recent wind-deposited snow, windpack, surface

hoar, sastrugi. For remote sensing purposes, the SSA and density values of the mean snow pit are probably relevant, given that the resolutions of satellites such as MODIS and AATSR are in the range 250 m to 1 km.

For the first part of the traverse (pits T1–T4), Fig. 14 indicates that the mean albedo is similar to that of the C group. This is consistent with the small differences in meteorological conditions and snow properties recorded between Dome C and the AWS at D85. From pit T5 and on, the role of wind and of the higher temperatures in determining snow physical properties is felt and the albedo is significantly different. It is clear that for the second part of the traverse, the number of pits performed is not sufficient to be a statistically valid sample, and clearly more studies are needed. Ideally, a science-dedicated traverse should be arranged. However, it seems very likely that the variations observed between the start and the end of the traverse are not explained by random variations, and that our observations represent a genuine change in snow physical properties.

To facilitate the comparison between our observations and satellite data by other researchers, we report in the Appendix Tables A3, A4 and A5 the data of our calculated albedos for the 5 light sources used, as a function of wavelength in the range 0.3–2.5 μm, for the C group, the T1–T4 group, and the T5–T8 group. For those readers who would require albedo data with a different fraction of diffuse radiation for SZA = 60 or 70°, it is possible to use the data of Appendix Tables A3 to A5 and the following equation:

$$a_{net} = R_{diffuse}a_d + (1 - R_{diffuse})a_s(\theta) \qquad (5)$$

where a_d is the diffuse albedo, a_s is the direct albedo, and the albedo is a_{net}.

3.9 Preliminary comparison with MODIS data

Table 3 reports the albedos calculated for the relevant MODIS and AATSR spectral bands. Below, we perform a preliminary comparison between MODIS data and our calculations under diffuse illumination. We used the "White Sky Albedo" (i.e. the albedo under diffuse illumination) of the MODIS product MCD43C3 (Version 5), which consists in 16-day averages calculated from data obtained under clear-sky conditions only. MCD43C3 data was used to obtain the albedo averaged over a square 25×25 km containing the location of our measurements. While a higher resolution product exists, using larger scale averages reduces noise and shows general trends more clearly. We compare here the MCD43C3 "White Sky Albedo" at Dome C and along the traverse to our calculations. For DC, we used the mean value of our 13 snow pits. Figures 16 and 17 show the results obtained for the 7 available wavelengths.

Some differences are observed but our results and the MODIS product show similar trends: the albedo, and hence the SSA, decrease from DC to the coast. Bands 2 (870 nm)

Table 3. Directional hemispherical reflectance of all mean pits calculated for the spectral bands of MODIS and AATSR satellites, and using the light sources of Table 2.

| λ, Satellite and bands	Incident source	Group C	T1–T4	T5–T8	λ, Satellite and bands	Incident source	Group C	T1–T4	T5–T8
470 nm, Modis band 3	DIR60	0.987	0.988	0.986	870 nm, AATSR and Modis band 2	DIR60	0.900	0.901	0.876
	DIR70	0.989	0.990	0.989		DIR70	0.916	0.917	0.896
	DIFF	0.985	0.986	0.984		DIFF	0.886	0.887	0.859
	CS60	0.988	0.988	0.985		CS60	0.900	0.900	0.876
	CS70	0.989	0.989	0.987		CS70	0.915	0.916	0.895
550 nm, AATSR and Modis band 4	DIR60	0.984	0.984	0.981	1240 nm, Modis band 5	DIR60	0.568	0.559	0.481
	DIR70	0.987	0.987	0.984		DIR70	0.627	0.619	0.547
	DIFF	0.982	0.983	0.979		DIFF	0.526	0.517	0.437
	CS60	0.984	0.985	0.981		CS60	0.567	0.559	0.480
	CS70	0.986	0.987	0.984		CS70	0.626	0.618	0.546
645 nm, Modis band 1	DIR60	0.970	0.973	0.966	1600 nm, AATSR	DIR60	0.120	0.114	0.071
	DIR70	0.975	0.978	0.972		DIR70	0.173	0.166	0.111
	DIFF	0.966	0.969	0.961		DIFF	0.104	0.099	0.063
	CS60	0.971	0.972	0.966		CS60	0.120	0.114	0.071
	CS70	0.975	0.976	0.971		CS70	0.173	0.166	0.111
660 nm, AATSR	DIR60	0.968	0.969	0.962	1640 nm, Modis band 6	DIR60	0.138	0.132	0.084
	DIR70	0.974	0.975	0.968		DIR70	0.195	0.188	0.129
	DIFF	0.963	0.965	0.956		DIFF	0.119	0.114	0.073
	CS60	0.967	0.969	0.962		CS60	0.138	0.132	0.084
	CS70	0.972	0.973	0.968		CS70	0.195	0.187	0.128
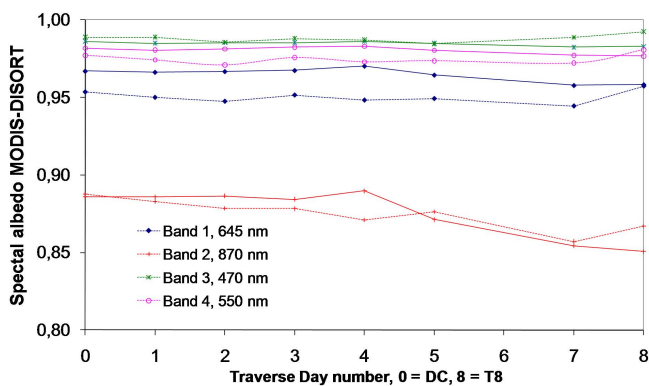
Fig. 16. Spatial variations of the spectral albedo during the traverse. Data shown compare values obtained for MODIS bands 1 to 4, with those calculated for the same wavelengths using DISORT and our snow SSA and density profiles (solid lines).
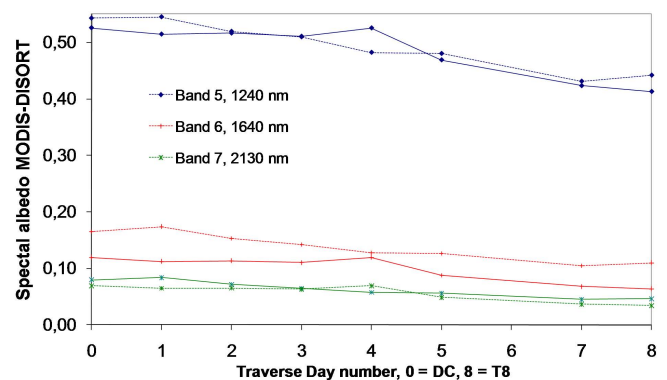
Fig. 17. Spatial variations of the spectral albedo during the traverse. Data shown compare values obtained for MODIS bands 5 to 7, with those calculated for the same wavelengths using DISORT and our snow SSA and density profiles (solid lines).

and 5 (1240 nm) are especially interesting because at those wavelengths snow reflectance is sensitive to the SSA.

The MCD43C3 product also provides a broadband albedo (0.3–5 µm). Greuell and Oerlemans (2004) propose an alternative method to determine the broadband albedo from MODIS bands 1, 2 and 4. We also used the parameterization

of Greuell and Oerlemans (2004) to obtain the broadband albedo from our calculated spectral albedos, using the values obtained for the relevant MODIS bands. The comparison between these three broadband albedos is shown in Fig. 18. All three methods clearly show the same trend and the absolute difference is on average of the order of 1 %. The agreement is
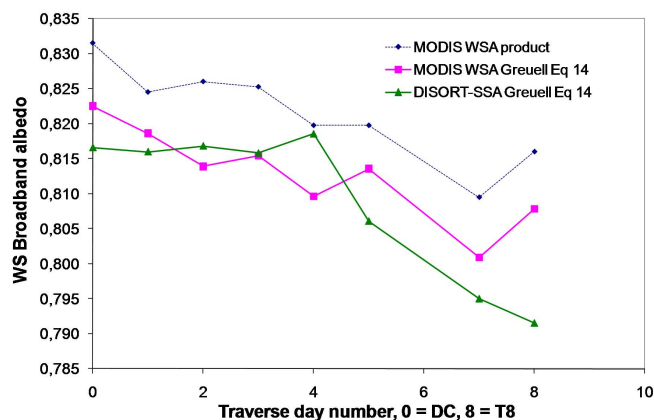
Fig. 18. Comparison of broadband albedos along the traverse calculated using three methods: (i) MODIS White Sky Albedo product; (ii) the empirical equation of Greuell and Oerlemans (2004) which uses MODIS data for bands 1, 2 and 4; (iii) the empirical equation of Greuell and Oerlemans (2004) using data for bands 1, 2 and 4 calculated from our snow data and DISORT.
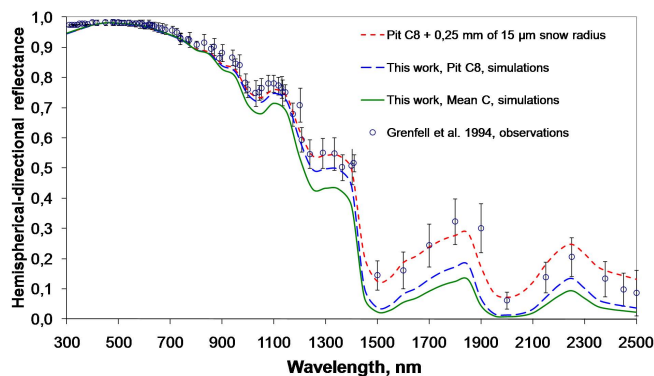
Fig. 19. Comparison between the reflectance of Grenfell et al. (1994) and that calculated from our snow data using DISORT and illumination and viewing conditions similar to those of Grenfell et al. (1994). Calculations using the stratigraphy of pit C8, to which a snow layer 0.25 mm thick with crystals 15 μm in radius match the observations of Grenfell et al. (1994) fairly well.

in fact surprisingly good given that MODIS and Greuell and Oerlemans (2004) use different bands to obtain the broadband albedo and that the formulas used are based on empirical fits from data obtained for the most part outside of the Antarctic plateau. The preliminary comparisons of Figs. 16 to 18 show reasonable agreements between MODIS products and our calculations based on SSA and density profiles. We consider this an encouraging sign to attempt to determine snow SSA from satellite observations.

Fig. 20. Calculated bi-hemispherical reflectance (i.e. albedo) of snow near Dome C, and comparison with the measurements of Hudson et al. (2006), performed under overcast conditions. Calculations using the stratigraphy of pit C8 match the observations of Hudson et al. (2006) fairly well. If a thin high-SSA layer is added, the albedo is much larger than observations in the IR.

4 Discussion

The data presented here are the first extensive SSA measurements of the surface snow on the Antarctic plateau. Brucker et al. (2011) recently published a single SSA profile of a 3 m-deep pit near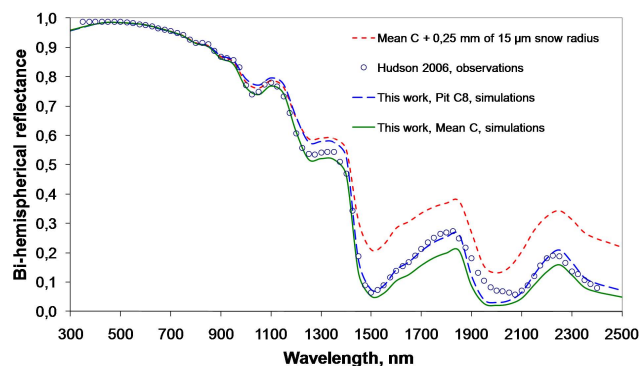 Dome C obtained using NIR photography. However, the relationship between their IR reflectance and SSA is not well established, and they test 3 relationships that predict significantly different SSAs. For example, for the topmost snow layer, the 3 methods predict SSA in the range 26 to 46 m² kg⁻¹. The objective of Brucker et al. (2011) is microwave application, and it is difficult to use their data for optical purposes. There has been very few albedo measurements on the Antarctic plateau performed under well characterized lighting conditions, so that they could be compared to our calculations. Grenfell et al. (1994) performed reflectance measurements at Vostok and South Pole stations. They show a graph of spectral albedo obtained at South Pole under diffuse illumination with nadir viewing (field of view 15°). Hudson et al. (2006) measured the bidirectional reflectance of the snow at Dome C. They show one spectral bihemispherical albedo (overcast sky) recorded on 30 December 2004. The following discussion focuses on both these studies. Since Grenfell et al. (1994) and Hudson et al. (2006) worked under different lighting conditions, two distinct graphs are necessary to compare their data to our calculations.

Figure 19 shows the data of Grenfell et al. (1994) and the albedo of the C8 pit and of the mean C pit, calculated for the lighting conditions of Grenfell et al. (1994). The albedo obtained by Grenfell et al. (1994) is significantly higher than ours in the IR. Grenfell et al. (1994) used their data to deduce optical grain sizes. They could not model their spectral reflectance with a single snow layer of a given grain size. They had to add a 0.25 mm-thick surface layer of density

$150 \, \mathrm{kg \, m^{-3}}$ and consisting of grains 15 to 30 µm in radius (SSA = 218 to 109 $\mathrm{m^2 \, kg^{-1}}$). In Fig. 19, we also show calculations where we have added a 0.25 mm-thick layer of grains 15 µm in radius at the very surface of the C8 stratigraphy. The agreement between the spectrum of Grenfell et al. (1994) and ours is pretty good.

However, we will stop short of over-interpreting the comparison between a spectrum measured at South Pole in 1986 and a spectrum calculated from snow properties measured at Dome C in 2009. Grenfell et al. (1994) justify the presence of the thin high-SSA layer at the top of the snow pack by wind action, suggesting that small particles will settle last after a wind event. Even if this is indeed the case, which we cannot judge here, it is not certain that this process would be as frequent at Dome C, which is significantly less windy than South Pole (Aristidi et al., 2005). Furthermore, errors in measurements of albedo, SSA, density and layer thickness and in modeling (DISORT does make approximations, in particular for directional viewing) are at least 20 %, so that comparing data obtained in two widely different settings is difficult. In particular, we feel that it is not reasonable to attempt any conclusion on the property of the very surface snow layer on the Antarctic Plateau with current data.

Hudson et al. (2006) measured the bidirectional reflectance of the snow at Dome C. They show one spectral bi-hemispherical albedo (overcast sky) recorded on 30 December 2004. They observed snow grains and mention that their visual size stayed in the range $r = 50$ to $100 \, \mu m$ (SSA = 33 to $65 \, \mathrm{m^2 \, kg^{-1}}$, if the grains are assumed to be spherical). Figure 20 compares their spectral albedo to calculated albedos under similar lighting and viewing conditions, for the mean C snow and for pit C8. Our albedo for pit C8 is very similar to that of Hudson et al. (2006). Calculations using the mean C snow to which a 0.25 mm-thick layer of SSA = 218 $\mathrm{m^2 \, kg^{-1}}$ ($r = 15 \, \mu m$) and density = 150 $\mathrm{kg \, m^{-3}}$ has been added yields much too high an albedo throughout the IR. Given that Hudson et al. (2006) only show one spectrum, there is clearly insufficient data to reach any conclusion on the possible existence of a thin high SSA layer at the top of Dome C snow. We strongly encourage further tests of the existence of a thin high-SSA layer at the very surface.

5 Conclusions

The data presented here are the first extensive measurements of SSA vertical profiles on the East Antarctic plateau. The concentration of impurities in the snow is sufficiently low not to affect albedo (Grenfell et al., 1994; Warren et al., 2006), and the SSA and density profiles that we obtained can therefore be used to calculate the hemispherical spectral albedo of the snow, if the effect of surface roughness can be neglected. The albedos thus obtained are, in the IR, lower than those of Grenfell et al. (1994) obtained in 1986 at South Pole. More data is required to assess the significance of this difference,

and its cause in terms of snow physical properties or uncertainties on measurements. The existence of a thin high SSA snow layer at the top of the snowpack at South Pole, postulated by Grenfell et al. (1994) is an interesting hypothesis that deserves further testing, as its consequences in terms of energy budget would be significant.

The calculated albedo of our mean Dome C snow pit is lower than the one spectral albedo of Hudson et al. (2006), but our pit with the highest calculated albedo agrees well with their data. Given the small number of data from Hudson et al. (2006) that can be compared to ours, insufficient representativity or variations in snow properties between 2004 and 2008–2009 may explain the difference.

A full understanding of snow physical properties and albedo would require combined measurements of albedo, with high resolution vertical profiles of SSA and density. Measuring the SSA of snow at several IR wavelengths having different penetration depths would be useful to detect a possible thin high-SSA layer at the surface. DUFISSS can in principle operate at both 1310 and 1550 nm, but at present the shorter wavelength has been calibrated for SSA < 66 $\mathrm{m^2 \, kg^{-1}}$, while the longer wavelength is calibrated for SSA > 50 $\mathrm{m^2 \, kg^{-1}}$. Further work to allow a greater overlap would be useful to this purpose. Lastly, our snow data allow the calculation of albedo that can be used to analyze remote sensing data and test inversion algorithms. Our preliminary investigations in fact show encouraging results regarding the possibility to determine SSA from space.

Appendix A

Table A1. SSAs and densities used in DISORT, group C.

Depth from top in cm	C1 SSA, m²kg⁻¹	Density, kgm⁻³	Snow Grains	C2 SSA, m²kg⁻¹	Density, kgm⁻³	Snow Grains	C3 (sastrugi on top 25 cm) SSA, m²kg⁻¹	Density, kgm⁻³	Snow Grains	C4 SSA, m²kg⁻¹	Density, kgm⁻³	Snow Grains	C5 SSA, m²kg⁻¹	Density, kgm⁻³	Snow Grains
1	52.9	305	RG	42.2	291	RG	32.7	227	RG+SH	41.6	158	SH	34.0	221	RG
2	52.9	305	RG	42.2	291	RG	24.8	216	RG+SH	27.9	314	WC	33.6	292	RG
5	52.9	305	RG	42.2	291	RG	36.8	363	WC	18.3	355	MF	33.6	292	RG
10	29.3	444	WC	25.5	368	WC	36.8	363	WC	18.3	355	MF	18.0	290	DH
15	15.1	353	MF	22.9	352	FC	27.6	368	WC	18.3	355	MF	17.4	290	DH
20	15.1	353	MF	20.8	336	FC	27.6	368	WC	19.2	355	MF	12.8	290	FC
30	16.6	341	MF	18.5	296	DH	25.1	328	MF	19.2	355	MF	14.4	318	FC
40	13.3	388	DH	11.9	317	DH	24.4	336	MF	16.2	316	FC	15.3	329	MF
50	11.8	328	DH	12.8	341	DH	24.6	339	MF	14.4	334	MF	11.0	352	DH
60	10.4	404	DH	12.8	371	DH	24.6	318	MF	15.9	334	MF	11.0	313	DH
70	10.4	404	DH	12.7	418	DH	28.1	353	WC	15.6	399	WC	11.8	315	DH

Depth from top in cm	C6 SSA, m²kg⁻¹	Density, kgm⁻³	Snow Grains	C7 (5 km from base) SSA, m²kg⁻¹	Density, kgm⁻³	Snow Grains	C8 (5 km from base) SSA, m²kg⁻¹	Density, kgm⁻³	Snow Grains	C9 (5 km from base) SSA, m²kg⁻¹	Density, kgm⁻³	Snow Grains	C10 SSA, m²kg⁻¹	Density, kgm⁻³	Snow Grains
1	40.3	298	WC	35.7	146	SH+RG	54.5	229	BR+Col+RG	40.6	293	RG	24.3	316	SH+FC
2	40.3	298	WC	27.7	222	RG+MF	16.6	229	FC+RG	30.3	293	RG+FC	24.3	316	SH+FC
5	29.6	298	MF	30.2	294	RG+MF	22.2	229	FC+RG	24.8	315	RG+FC	13.0	466	MF
10	22.2	356	RG+MF	29.5	297	RG+MF	24.1	306	WC	26.0	315	RG+FC	27.7	454	WC
15	21.6	356	RG+MF	33.1	297	RG+MF	22.3	466	WC	19.7	460	WC	18.3	466	WC
20	19.1	356	RG+MF	38.8	306	RG+MF	19.2	466	WC	15.4	307	MF+DH	19.7	466	WC
30	16.8	326	MF	39.3	384	RG+MF	14.5	322	DH	14.3	307	MF+DH	17.9	508	WC
40	16.1	326	MF	26.8	446	WC	14.8	310	DH	14.3	349	MF+DH	15.9	521	FC
50	16.0	363	MF	18.2	380	MF	14.7	347	MF	10.7	343	DH	12.4	343	FC
60	14.0	347	MF	18.2	340	MF	15.6	347	MF	10.7	333	DH	10.2	312	DH
70	11.7	343	MF	13.4	310	MF	12.9	325	MF	10.1	313	DH	12.0	274	DH

Depth from top in cm	C11 SSA, m²kg⁻¹	Density, kgm⁻³	Snow Grains	C12 (25 km South from base) SSA, m²kg⁻¹	Density, kgm⁻³	Snow Grains	C13 (25 km north from base) SSA, m²kg⁻¹	Density, kgm⁻³	Snow Grains	Mean all pits C SSA, m²kg⁻¹	Density, kgm⁻³	Snow grains meaning Notation	Snow Grains
1	41.1	260	SH	26.0	334	RG	29.7	317	WC	38.1	261	BR	Bullet Rosette
2	40.5	291	RG	26.0	334	RG	26.0	317	WC	31.8	286	Col	Column
5	46.1	260	RG	26.0	334	RG	26.0	317	WC	30.9	317	DH	Depth Hoar
10	19.8	321	MF	25.5	334	RG	29.4	317	RG+SH	25.5	355	FC	Faceted Crystal
15	19.8	352	MF	25.5	334	MF	29.4	317	RG+SH	22.4	374	MF	Mixed Form
20	15.8	333	MF	26.7	330	MF	24.8	356	RG+SH	21.2	363	RG	Rounded Grain
30	12.9	359	MF	24.0	330	FC	21.1	356	MF	19.6	348	SH	Surface Hoar
40	11.3	348	MF+DH	17.3	330	DH	21.1	356	MF	16.8	359	WC	Wind Crust
50	11.1	363	MF+DH	13.7	348	DH	12.7	332	DH	14.2	347		
60	10.0	317	MF+DH	13.7	348	DH	12.7	332	DH	13.8	340		
70	11.9	310	MF+DH	13.7	348	DH	12.7	332	DH	13.6	342		

Table A2. SSAs and densities values used in DISORT, group T.

Depth from top in cm	T1 SSA, m²kg⁻¹	Density, kgm⁻³	Snow Grains	T2 SSA, m²kg⁻¹	Density, kgm⁻³	Snow Grains	T3 SSA, m²kg⁻¹	Density, kgm⁻³	Snow Grains	T4 SSA, m²kg⁻¹	Density, kgm⁻³	Snow Grains	Mean T1–T4 SSA, m²kg⁻¹	Density, kgm⁻³
1	35.6	162	RG	36.0	351	WC	34.8	285	SH+RG	38.0	407	WC	36.1	301
2	35.6	162	RG	36.0	351	WC	34.8	285	RG	38.0	407	WC	36.1	301
5	35.6	162	RG	36.0	351	WC	34.8	285	RG	38.0	407	WC	36.1	301
10	31.6	150	WC	20.1	302	MF	27.9	400	WC	38.0	407	WC	29.4	315
15	20.7	208	FC	23.4	353	WC	30.0	403	WC	22.8	341	FC	24.2	326
20	20.7	208	FC	18.6	353	FC	18.5	355	MF	22.8	341	FC	20.2	314
30	14.4	251	FC	20.3	353	FC	16.0	341	FC	23.4	380	WC	18.5	331
40	17.0	277	FC	24.0	325	FC	12.0	330	FC+DH	23.3	380	MF	19.1	328
50	14.2	272	FC+DH	15.0	325	FC	14.4	382	FC+DH	23.2	381	MF	16.7	340
60	13.0	278	FC+DH	15.0	325	FC	X	X	X	X	X	X	14.0	302
70	13.1	287	FC+DH	14.3	335	FC	X	X	X	X	X	X	13.7	311

Depth from top in cm	T5 SSA, m²kg⁻¹	Density, kgm⁻³	Snow Grains	T7 SSA, m²kg⁻¹	Density, kgm⁻³	Snow Grains	T8 SSA, m²kg⁻¹	Density, kgm⁻³	Snow Grains	Mean T5–T8 SSA, m²kg⁻¹	Density, kgm⁻³	Snow grains meaning Notation	Snow Grains
1	27.3	415	WC	21.0	374	WC	19.8	446	WC	22.7	412	DH	Depth Hoar
2	27.3	415	WC	21.0	374	WC	19.8	446	WC	22.7	412	FC	Faceted Crystal
5	27.3	415	WC	21.0	374	WC	19.8	446	WC	22.7	412	MF	Mixed Form
10	22.5	399	RG	16.0	515	WC	16.7	463	FC	18.4	459	RG	Rounded Grain
15	22.5	399	RG	16.0	515	WC	18.9	464	WC	19.1	459	SH	Surface Hoar
20	22.7	337	RG	16.0	486	WC	18.4	497	FC	19.0	440	WC	Wind Crust
30	23.2	370	MF	16.0	506	WC	17.6	477	FC	18.9	451		
40	23.7	403	MF	16.4	509	WC	X	X	X	20.1	456		
50	23.7	403	MF	16.6	478	WC	X	X	X	20.2	441		
60	X	X	X	17.7	459	FC	X	X	X	17.7	459		
70	X	X	X	16.5	473	WC	X	X	X	16.5	473		

Table A3. Directional hemispherical reflectance of the mean of group C pits, at Dome C, calculated using the light sources of Table 2.

λ, nm	DIR60	DIR70	DIFF	CS60	CS70	λ, nm	DIR60	DIR70	DIFF	CS60	CS70
					DOME C, Group C						
300	0.964	0.970	0.958	0.964	0.970	1450	0.147	0.206	0.127	0.147	0.205
350	0.974	0.978	0.970	0.974	0.978	1500	0.057	0.092	0.051	0.057	0.091
400	0.982	0.985	0.979	0.982	0.985	1550	0.070	0.109	0.061	0.069	0.109
450	0.987	0.989	0.985	0.987	0.988	1600	0.120	0.173	0.104	0.120	0.173
500	0.986	0.989	0.984	0.986	0.987	1650	0.145	0.203	0.125	0.145	0.203
550	0.984	0.987	0.982	0.984	0.986	1700	0.181	0.245	0.156	0.181	0.245
600	0.979	0.983	0.976	0.979	0.982	1750	0.211	0.278	0.182	0.211	0.277
650	0.970	0.975	0.966	0.970	0.974	1800	0.229	0.297	0.198	0.229	0.297
700	0.961	0.967	0.954	0.959	0.965	1850	0.238	0.307	0.207	0.238	0.307
750	0.946	0.955	0.939	0.946	0.954	1900	0.100	0.149	0.087	0.100	0.148
800	0.924	0.936	0.913	0.924	0.935	1950	0.028	0.049	0.026	0.028	0.049
850	0.914	0.928	0.902	0.914	0.927	2000	0.021	0.038	0.020	0.021	0.037
900	0.879	0.898	0.862	0.878	0.897	2050	0.026	0.046	0.024	0.026	0.046
950	0.861	0.884	0.842	0.861	0.882	2100	0.049	0.080	0.044	0.049	0.080
1000	0.791	0.823	0.763	0.790	0.822	2150	0.103	0.153	0.090	0.103	0.153
1050	0.768	0.804	0.739	0.767	0.802	2200	0.155	0.216	0.134	0.155	0.215
1100	0.795	0.827	0.768	0.794	0.826	2250	0.184	0.248	0.158	0.184	0.248
1150	0.771	0.806	0.742	0.771	0.805	2300	0.143	0.202	0.124	0.143	0.202
1200	0.651	0.701	0.612	0.650	0.700	2350	0.093	0.141	0.082	0.093	0.141
1250	0.560	0.620	0.518	0.560	0.619	2400	0.074	0.117	0.066	0.074	0.117
1300	0.563	0.622	0.520	0.562	0.621	2450	0.064	0.102	0.057	0.064	0.102
1350	0.560	0.620	0.518	0.560	0.619	2500	0.053	0.088	0.048	0.053	0.088
1400	0.509	0.573	0.465	0.508	0.572						

Table A4. Directional hemispherical reflectance of the mean of pits T1 to T4, calculated using the light sources of Table 2.

λ, nm	DIR60	DIR70	DIFF	CS60	CS70	λ, nm	DIR60	DIR70	DIFF	CS60	CS70
					LOGISTIC TRAVERSE, T1–T4						
300	0.965	0.971	0.959	0.964	0.970	1450	0.140	0.198	0.121	0.140	0.197
350	0.975	0.979	0.971	0.975	0.979	1500	0.054	0.087	0.048	0.054	0.087
400	0.983	0.986	0.981	0.983	0.986	1550	0.066	0.104	0.058	0.065	0.103
450	0.988	0.990	0.985	0.986	0.988	1600	0.114	0.166	0.099	0.114	0.166
500	0.987	0.989	0.985	0.987	0.988	1650	0.138	0.195	0.119	0.138	0.195
550	0.984	0.987	0.983	0.985	0.987	1700	0.174	0.236	0.150	0.174	0.236
600	0.981	0.984	0.978	0.980	0.983	1750	0.203	0.269	0.175	0.202	0.268
650	0.972	0.977	0.968	0.972	0.976	1800	0.220	0.288	0.191	0.220	0.288
700	0.962	0.968	0.955	0.961	0.967	1850	0.230	0.298	0.199	0.230	0.298
750	0.948	0.956	0.941	0.948	0.956	1900	0.094	0.142	0.082	0.094	0.142
800	0.926	0.938	0.915	0.925	0.937	1950	0.027	0.046	0.025	0.027	0.046
850	0.916	0.930	0.904	0.915	0.928	2000	0.020	0.035	0.019	0.020	0.035
900	0.879	0.898	0.862	0.878	0.897	2050	0.025	0.043	0.023	0.025	0.043
950	0.861	0.883	0.842	0.860	0.882	2100	0.046	0.076	0.041	0.046	0.076
1000	0.787	0.820	0.760	0.786	0.819	2150	0.097	0.146	0.085	0.097	0.146
1050	0.763	0.800	0.734	0.763	0.798	2200	0.148	0.207	0.128	0.148	0.207
1100	0.791	0.824	0.764	0.791	0.823	2250	0.176	0.239	0.152	0.176	0.239
1150	0.767	0.803	0.738	0.766	0.802	2300	0.136	0.194	0.118	0.136	0.194
1200	0.643	0.694	0.605	0.643	0.693	2350	0.088	0.135	0.077	0.088	0.135
1250	0.552	0.612	0.509	0.551	0.611	2400	0.070	0.111	0.062	0.070	0.111
1300	0.554	0.614	0.511	0.554	0.613	2450	0.060	0.097	0.053	0.060	0.097
1350	0.552	0.612	0.509	0.551	0.611	2500	0.050	0.083	0.045	0.050	0.083
1400	0.499	0.564	0.456	0.499	0.563						

Table A5. Directional hemispherical reflectance of the mean of pits T5 to T8, calculated using the light sources of Table 2.

						LOGISTIC TRAVERSE, T5–T8					
λ, nm	DIR60	DIR70	DIFF	CS60	CS70	λ, nm	DIR60	DIR70	DIFF	CS60	CS70
300	0.956	0.964	0.949	0.956	0.963	1450	0.090	0.137	0.079	0.090	0.137
350	0.968	0.974	0.964	0.969	0.974	1500	0.031	0.054	0.028	0.031	0.053
400	0.980	0.983	0.977	0.980	0.983	1550	0.039	0.065	0.035	0.038	0.065
450	0.985	0.988	0.984	0.985	0.987	1600	0.071	0.111	0.063	0.071	0.111
500	0.984	0.987	0.983	0.985	0.987	1650	0.089	0.135	0.077	0.089	0.134
550	0.981	0.984	0.979	0.981	0.984	1700	0.116	0.169	0.100	0.116	0.169
600	0.976	0.980	0.972	0.976	0.979	1750	0.139	0.197	0.119	0.139	0.196
650	0.965	0.971	0.960	0.964	0.970	1800	0.153	0.214	0.132	0.153	0.214
700	0.952	0.960	0.945	0.952	0.959	1850	0.161	0.223	0.139	0.161	0.222
750	0.935	0.946	0.925	0.934	0.944	1900	0.057	0.093	0.051	0.057	0.093
800	0.907	0.922	0.893	0.906	0.920	1950	0.015	0.027	0.014	0.015	0.027
850	0.896	0.913	0.880	0.894	0.911	2000	0.012	0.021	0.011	0.012	0.021
900	0.850	0.874	0.829	0.849	0.872	2050	0.014	0.025	0.013	0.014	0.025
950	0.827	0.854	0.804	0.827	0.853	2100	0.026	0.046	0.024	0.026	0.046
1000	0.739	0.779	0.708	0.739	0.777	2150	0.059	0.096	0.053	0.059	0.096
1050	0.711	0.754	0.677	0.710	0.753	2200	0.095	0.144	0.083	0.095	0.144
1100	0.744	0.783	0.713	0.743	0.782	2250	0.117	0.171	0.101	0.117	0.171
1150	0.715	0.758	0.681	0.715	0.757	2300	0.087	0.133	0.076	0.087	0.133
1200	0.573	0.632	0.531	0.573	0.630	2350	0.053	0.087	0.047	0.053	0.087
1250	0.473	0.539	0.429	0.472	0.538	2400	0.041	0.070	0.037	0.041	0.070
1300	0.475	0.542	0.431	0.475	0.541	2450	0.034	0.060	0.032	0.034	0.060
1350	0.473	0.539	0.428	0.472	0.538	2500	0.028	0.051	0.026	0.028	0.051
1400	0.417	0.487	0.374	0.417	0.486						

References

Alley, R. B.: Firn densification by grain-boundary sliding – a 1st model, J. Phys.-Paris, 48, 249–256, 1987.

Aoki, T., Fukabori, M., Hachikubo, A., Tachibana, Y., and Nishio, F.: Effects of snow physical parameters on spectral albedo and bidirectional reflectance of snow surface, J. Geophys. Res.-Atmos., 105, 10219–10236, 2000.

Aristidi, E., Agabi, K., Azouit, M., Fossat, E., Vernin, J., Travouillon, T., Lawrence, J. S., Meyer, C., Storey, J. W. V., Halter, B., Roth, W. L., and Walden, V.: An analysis of temperatures and wind speeds above Dome C, Antarctica, Astron. Astrophys., 430, 739–746, doi:10.1051/0004-6361:20041876, 2005.

Arnaud, L., Picard, G., Champollion, N., Domine, F., Gallet, J., Lefebvre, E., Fily, M., and Barnola, J. M.: Measurement of vertical profiles of snow specific surface area with a one centimeter resolution using infrared reflectance: Instrument description and validation, J. Glaciol., 57, 17–29, 2011.

Brucker, L., Picard, G., Arnaud, L., Barnola, J. M., Schneebeli, M., Brunjail, H., Lefebvre, E., and Fily, M.: Modeling time series of microwave brightness temperature at Dome C, Antarctica, using vertically resolved snow temperature and microstructure measurements, J. Glaciol., 57, 171–182, 2011.

Burniston, D. A., Strachan, W. J. M., Hoff, J. T., and Wania, F.: Changes in surface area and concentrations of semivolatile organic contaminants in aging snow, Environ. Sci. Technol., 41, 4932–4937, doi:10.1021/es0706450, 2007.

Cabanes, A., Legagneux, L., and Domine, F.: Evolution of the specific surface area and of crystal morphology of Arctic fresh snow during the ALERT 2000 campaign, Atmos. Environ., 36, 2767–2777, 2002.

Cabanes, A., Legagneux, L., and Domine, F.: Rate of evolution of the specific surface area of surface snow layers, Environ. Sci. Technol., 37, 661–666, doi:10.1021/es025880r, 2003.

Colbeck, S. C.: An overview of seasonal snow metamorphism, Rev. Geophys., 20, 45–61, 1982.

Conger, S. M. and McClung, D. M.: Comparison of density cutters for snow profile observations, J. Glaciol., 55, 163–169, 2009.

Cox, R. A., Fernandez, M. A., Symington, A., Ullerstam, M., and Abbatt, J. P. D.: A kinetic model for uptake of HNO3 and HCl on ice in a coated wall flow system, Phys. Chem. Chem. Phys., 7, 3434–3442, doi:10.1039/b506683b, 2005.

Domine, F. and Shepson, P. B.: Air-snow interactions and atmospheric chemistry, Science, 297, 1506–1510, 2002.

Domine, F. and Thibert, E.: Mechanism of incorporation of trace gases in ice grown from the gas phase, Geophys. Res. Lett., 23, 3627–3630, 1996.

Domine, F., Thibert, E., Silvente, E., Legrand, M., and Jaffrezo, J. L.: Determining past atmospheric HCl mixing ratios from ice core analyses, J. Atmos. Chem., 21, 165–186, 1995.

Domine, F., Salvatori, R., Legagneux, L., Salzano, R., Fily, M., and Casacchia, R.: Correlation between the specific surface area and the short wave infrared (SWIR) reflectance of snow, Cold Reg. Sci. Technol., 46, 60–68, doi:10.1016/j.coldregions.2006.06.002, 2006.

Domine, F., Cincinelli, A., Bonnaud, E., Martellini, T., and Picaud, S.: Adsorption of phenanthrene on natural snow, Environ. Sci. Technol., 41, 6033–6038, doi:10.1021/es0706798, 2007a.

Domine, F., Taillandier, A. S., and Simpson, W. R.: A

parameterization of the specific surface area of seasonal snow for field use and for models of snowpack evolution, J. Geophys. Res.-Earth, 112, F02031, doi:10.1029/2006jf000512, 2007b.

Domine, F., Albert, M., Huthwelker, T., Jacobi, H.-W., Kokhanovsky, A. A., Lehning, M., Picard, G., and Simpson, W. R.: Snow physics as relevant to snow photochemistry, Atmos. Chem. Phys., 8, 171–208, doi:10.5194/acp-8-171-2008, 2008.

Domine, F., Taillandier, A.-S., Cabanes, A., Douglas, T. A., and Sturm, M.: Three examples where the specific surface area of snow increased over time, The Cryosphere, 3, 31–39, doi:10.5194/tc-3-31-2009, 2009.

Fily, M., Bourdelles, B., Dedieu, J. P., and Sergent, C.: Comparison of in situ and Landsat thematic mapper derived snow grain characteristics in the Alps, Remote Sens. Environ., 59, 452–460, 1997.

Flanner, M. G. and Zender, C. S.: Linking snowpack microphysics and albedo evolution, J. Geophys. Res.-Atmos., 111, D12208, doi:10.1029/2005jd006834, 2006.

Frezzotti, M., Pourchet, M., Flora, O., Gandolfi, S., Gay, M., Urbini, S., Vincent, C., Becagli, S., Gragnani, R., Proposito, M., Severi, M., Traversi, R., Udisti, R., and Fily, M.: Spatial and temporal variability of snow accumulation in East Antarctica from traverse data, J. Glaciol., 51, 113–124, 2005.

Gallet, J.-C., Domine, F., Zender, C. S., and Picard, G.: Measurement of the specific surface area of snow using infrared reflectance in an integrating sphere at 1310 and 1550 nm, The Cryosphere, 3, 167–182, doi:10.5194/tc-3-167-2009, 2009.

Goody, R.: Polar process and world climate (a brief overview), Mon. Weather Rev., 108, 1935–1942, 1980.

Grannas, A. M., Jones, A. E., Dibb, J., Ammann, M., Anastasio, C., Beine, H. J., Bergin, M., Bottenheim, J., Boxe, C. S., Carver, G., Chen, G., Crawford, J. H., Dominé, F., Frey, M. M., Guzmán, M. I., Heard, D. E., Helmig, D., Hoffmann, M. R., Honrath, R. E., Huey, L. G., Hutterli, M., Jacobi, H. W., Klán, P., Lefer, B., McConnell, J., Plane, J., Sander, R., Savarino, J., Shepson, P. B., Simpson, W. R., Sodeau, J. R., von Glasow, R., Weller, R., Wolff, E. W., and Zhu, T.: An overview of snow photochemistry: evidence, mechanisms and impacts, Atmos. Chem. Phys., 7, 4329–4373, doi:10.5194/acp-7-4329-2007, 2007.

Grenfell, T. C. and Warren, S. G.: Representation of a nonspherical ice particle by a collection of independent spheres for scattering and absorption of radiation, J. Geophys. Res.-Atmos., 104, 31697–31709, 1999.

Grenfell, T. C., Warren, S. G., and Mullen, P. C.: Reflection of solar-radiation by the Antarctic snow surface at ultraviolet, visible, and near-infrared wavelengths, J. Geophys. Res.-Atmos., 99, 18669–18684, 1994.

Grenfell, T. C., Neshyba, S. P., and Warren, S. G.: Representation of a nonspherical ice particle by a collection of independent spheres for scattering and absorption of radiation: 3. Hollow columns and plates, J. Geophys. Res.-Atmos., 110, D17203, doi:10.1029/2005jd005811, 2005.

Greuell, W. and Oerlemans, J.: Narrowband-to-broadband albedo conversion for glacier ice and snow: equations based on modeling and ranges of validity of the equations, Remote Sens. Environ., 89, 95–105, doi:10.1016/j.rse.2003.10.010, 2004.

Hall, A.: The role of surface albedo feedback in climate, J. Climate, 17, 1550–1568, 2004.

Herbert, B. M. J., Villa, S., and Halsall, C.: Chemical interactions with snow: Understanding the behavior and fate of semi-volatile organic compounds in snow, Ecotox. Environ. Safe., 63, 3–16, 2006.

Houdier, S., Perrier, S., Domine, F., Cabanes, A., Legagneux, L., Grannas, A. M., Guimbaud, C., Shepson, P. B., Boudries, H., and Bottenheim, J. W.: Acetaldehyde and acetone in the Arctic snowpack during the ALERT2000 campaign. Snowpack composition, incorporation processes and atmospheric impact, Atmos. Environ., 36, 2609–2618, 2002.

Hudson, S. R., Warren, S. G., Brandt, R. E., Grenfell, T. C., and Six, D.: Spectral bidirectional reflectance of Antarctic snow: Measurements and parameterization, J. Geophys. Res.-Atmos., 111, D18106, doi:10.1029/2006jd007290, 2006.

Jin, Z. H., Charlock, T. P., Yang, P., Xie, Y., and Miller, W.: Snow optical properties for different particle shapes with application to snow grain size retrieval and MODIS/CERES radiance comparison over Antarctica, Remote Sens. Environ., 112, 3563–3581, doi:10.1016/j.rse.2008.04.011, 2008.

Kokhanovsky, A. and Schreier, M.: The determination of snow specific surface area, albedo and effective grain size using AATSR space-borne measurements, Int. J. Remote Sens., 30, 919–933, doi:10.1080/01431160802395250, 2009.

Kokhanovsky, A. A. and Zege, E. P.: Scattering optics of snow, Appl. Optics, 43, 1589–1602, 2004.

Legagneux, L. and Domine, F.: A mean field model of the decrease of the specific surface area of dry snow during isothermal metamorphism, J. Geophys. Res.-Earth, 110, F04011, doi:10.1029/2004jf000181, 2005.

Legagneux, L., Cabanes, A., and Domine, F.: Measurement of the specific surface area of 176 snow samples using methane adsorption at 77 K, J. Geophys. Res.-Atmos., 107, 4335, doi:10.1029/2001jd001016, 2002.

Legagneux, L., Taillandier, A. S., and Domine, F.: Grain growth theories and the isothermal evolution of the specific surface area of snow, J. Appl. Phys., 95, 6175–6184, doi:10.1063/1.1710718, 2004.

Lemke, P., Ren, J., Alley, R. B., Allison, I., Carrasco, J., Flato, G., Fujii, Y., Kaser, G., Mote, P., Thomas, R. H., and Zhang, T.: Observations Changes in Snow, Ice and Frozen Ground, in: Climate Change 2007: The physical Sciences Basis, edited by: Pachauri, R. K. and Reisinger, A., IPCC, Geneva, Switzerland, 2007.

Leroux, C. and Fily, M.: Modeling the effect of sastrugi on snow reflectance, J. Geophys. Res.-Planet., 103, 25779–25788, 1998.

Lyapustin, A., Tedesco, M., Wang, Y. J., Aoki, T., Hori, M., and Kokhanovsky, A.: Retrieval of snow grain size over Greenland from MODIS, Remote Sens. Environ., 113, 1976–1987, doi:10.1016/j.rse.2009.05.008, 2009.

Matzl, M. and Schneebeli, M.: Measuring specific surface area of snow by near-infrared photography, J. Glaciol., 52, 558–564, 2006.

Mondet, J. and Fily, M.: The reflectance of rough snow surfaces in Antarctica from POLDER/ADEOS remote sensing data, Geophys. Res. Lett., 26, 3477–3480, 1999.

Neshyba, S. P., Grenfell, T. C., and Warren, S. G.: Representation of a nonspherical ice particle by a collection of independent spheres for scattering and absorption of radiation: 2. Hexagonal columns and plates, J. Geophys. Res.-Atmos., 108, D15, doi:10.1029/2002jd003302, 2003.

Painter, T. H., Molotch, N. P., Cassidy, M., Flanner, M., and Steffen, K.: Instruments and methods – Contact spectroscopy for determination of stratigraphy of snow optical grain size, J. Glaciol., 53, 121–127, 2007.

Picard, G., Arnaud, L., Domine, F., and Fily, M.: Determining snow specific surface area from near-infrared reflectance measurements: Numerical study of the influence of grain shape, Cold Reg. Sci. Technol., 56, 10–17, doi:10.1016/j.coldregions.2008.10.001, 2009.

Pinzer, B. R. and Schneebeli, M.: Snow metamorphism under alternating temperature gradients: Morphology and recrystallization in surface snow, Geophys. Res. Lett., 36, L23503, doi:10.1029/2009gl039618, 2009.

Scambos, T. A., Haran, T. M., Fahnestock, M. A., Painter, T. H., and Bohlander, J.: MODIS-based Mosaic of Antarctica (MOA) data sets: Continent-wide surface morphology and snow grain size, Remote Sens. Environ., 111, 242–257, doi:10.1016/j.rse.2006.12.020, 2007.

Schaepman-Strub, G., Schaepman, M. E., Painter, T. H., Dangel, S., and Martonchik, J. V.: Reflectance quantities in optical remote sensing-definitions and case studies, Remote Sens. Environ., 103, 27–42, doi:10.1016/j.rse.2006.03.002, 2006.

Stamnes, K., Tsay, S. C., Wiscombe, W., and Jayaweera, K.: Numerically stable algorithm for discrete-ordinate-method radiative-transfer in multiple-scattering and emitting layered media, Appl. Optics, 27, 2502–2509, 1988.

Stroeve, J. C. and Nolin, A. W.: New methods to infer snow albedo from the MISR instrument with applications to the Greenland ice sheet, IEEE T. Geosci. Remote, 40, 1616–1625, doi:10.1109/tgrs.2002.801144, 2002.

Taillandier, A. S., Domine, F., Simpson, W. R., Sturm, M., Douglas, T. A., and Severin, K.: Evolution of the snow area index of the subarctic snowpack in central Alaska over a whole season. Consequences for the air to snow transfer of pollutants, Environ. Sci. Technol., 40, 7521–7527, doi:10.1021/es060842j, 2006.

Taillandier, A. S., Domine, F., Simpson, W. R., Sturm, M., and Douglas, T. A.: Rate of decrease of the specific surface area of dry snow: Isothermal and temperature gradient conditions, J. Geophys. Res.-Earth, 112, F03003, doi:10.1029/2006jf000514, 2007.

Warren, S. G.: Optical-properties of snow, Rev. Geophys., 20, 67–89, 1982.

Warren, S. G. and Clarke, A. D.: Soot in the atmosphere and snow surface of Antarctica, J. Geophys. Res.-Atmos., 95, 1811–1816, 1990.

Warren, S. G. and Wiscombe, W. J.: A model for the spectral albedo of snow. 2. Snow containing atmospheric aerosols, J. Atmos. Sci., 37, 2734–2745, 1980.

Warren, S. G., Brandt, R. E., and Hinton, P. O.: Effect of surface roughness on bidirectional reflectance of Antarctic snow, J. Geophys. Res.-Planet., 103, 25789–25807, 1998.

Warren, S. G., Brandt, R. E., and Grenfell, T. C.: Visible and near-ultraviolet absorption spectrum of ice from transmission of solar radiation into snow, Appl. Optics, 45, 5320–5334, 2006.

Wiscombe, W. J.: Improved Mie scattering algorithms, Appl. Optics, 19, 1505–1509, 1980.

Wiscombe, W. J. and Warren, S. G.: A model for the spectral albedo of snow. 1. Pure snow, J. Atmos. Sci., 37, 2712–2733, 1980.

Zhou, X. B., Li, S. S., and Stamnes, K.: Effects of vertical inhomogeneity on snow spectral albedo and its implication for optical remote sensing of snow, J. Geophys. Res.-Atmos., 108, D4738, doi:10.1029/2003jd003859, 2003.